Dynamical symmetry and valley-selective circularly polarized high-harmonic generation in monolayer molybdenum disulfide

Yong-Lin He,[1,2,3,*] Jing Guo,[1,†] Fang-Yan Gao,[1] and Xue-Shen Liu[1]
[1]*Institute of Atomic and Molecular Physics, Jilin University, Changchun 130012, China*
[2]*School of Physics and Electromechanical Engineering, Hexi University, Zhangye 734000, China*
[3]*Institute of Theoretical Physics, Hexi University, Zhangye 734000, China*

(Received 18 October 2021; revised 23 December 2021; accepted 11 January 2022; published 21 January 2022)

Circularly polarized high harmonics (CHHs) have been observed in several solid targets under single-color circularly polarized excitation. However, experimental observations show that CHHs cannot be efficiently generated in monolayer molybdenum disulphide (MoS_2) driving by a single-color circularly polarized laser, thus letting its unique valley-selective circular dichroism (VSCD) to remain unexploited in the high harmonic generation process. Here we demonstrate that the efficient generation of CHHs in monolayer MoS_2 driven by counterrotating bicircular (CRB) fields and the broken inversion symmetry of monolayer MoS_2 leads to the generation of forbidden $3n$ ($n \in \mathbb{N}$) harmonic orders. Interestingly, we find that the VSCD lead to a distinctive valley selection of harmonic orders, while the valley selection caused by the trefoil orientation relative to the lattice is also observed. Dynamical symmetry analyses show that the rotational symmetry of the crystals can be decoded by the combination of a linearly polarized excitation scheme and CRB excitation scheme via the lowest common multiple rule. Additionally, VSCD leaves unique fingerprints in the ellipticity of harmonics.

DOI: 10.1103/PhysRevB.105.024305

I. INTRODUCTION

Circularly polarized high harmonics (CHHs) play an important role in investigating chirality-sensitive light matter interactions [1–6]. Due to the recollision-based mechanism, generating CHHs directly in the gas-phase relies on counterrotating bicircular (CRB) pulses [5,7,8], noncollinear counterrotating circularly polarized fields [9], or the use of molecular alignment techniques [10]. In contrast, the periodic nature and the accompanying band structure of the crystalline solid leads to an intrinsically different mechanism of high harmonic generation (HHG) from a solid. The anisotropy of the band structure and the easy-to-control direction of the crystal axis are conducive to the generation, measurement, and control of the polarized harmonic radiation. Several experiments reported the polarization properties of the harmonics from solids [11–18]. The generation of CHHs has been theoretical predicted in cubic Si and MgO excited by single-color circularly polarized (CP) pulses [19]. Experimentally, CHHs were obtained in a thin gallium selenide crystal [20] and quartz [21] irradiated by CP pulses. Recently, it was shown that the polarization states of high harmonics from solids can differ from those of the drivers [17,18], CHHs with elliptically polarized (EP) excitation were observed experimentally in cubic Si [17] and zinc-blende ZnS [18].

The negligible propagation effect, unique energy band structure, and distinctive optical properties make two-dimensional (2D) materials interesting candidates for HHG [12,22–33]. For HHG in the 2D target driving by midinfrared pulses, both atomic-like [22,31] and anomalous ellipticity dependence (harmonic yields are enhanced by elliptically polarized driver) [23,24] are experimentally or theoretically observed. These results illustrate the important point that harmonic yields are greatly suppressed by using a CP driving field. Theoretical simulation shows that it is possible to generate CHHs in graphene with a single CP, near-infrared driver [25], or CRB fields, composed of the fundamental and its second harmonic [26]. Some theoretical results even show that the linearly polarized (LP) driver lead to the emission of elliptically polarized high harmonics (EHHs), on the contrary, EP driver may give rise to LP harmonics [27].

Monolayer molybdenum disulphide (MoS_2) can be regarded as the semiconductor analog of graphene. Unlike the bulk MoS_2 with indirect band gap, monolayer MoS_2 crystal is a direct band-gap semiconductor (1.8 eV) with hexagonal lattice structure [34]. The first Brillouin zone (BZ) with two nonorthogonal primitive reciprocal vectors $\mathbf{b}_1$ and $\mathbf{b}_2$ and the associated high-symmetric points are shown in Fig. 1(b). The two local minima of the band gap shown in Fig. 1(a) are the valleys. The broken inversion symmetry induces positive (negative) Berry curvature in K valley (K' valley). More importantly, the broken inversion symmetry also gives rise to a unique valley-selective circular dichroism (VSCD) [Fig. 1(d)] [35–38], that is, the K valley only absorbs left circularly polarized photons, whereas the K' valley absorbs right circularly polarized photons [35,36]. The VSCD is quantified by the k-resolved degree of circular polarization (DCP) shown in Fig. 1(c) [34,36]. The unique VSCD is expected to play an important role in the generation of CHHs in monolayer MoS_2. However, for the monolayer MoS_2 crystal, both the

*hyl@hxu.edu.cn
†gjing@jlu.edu.cn

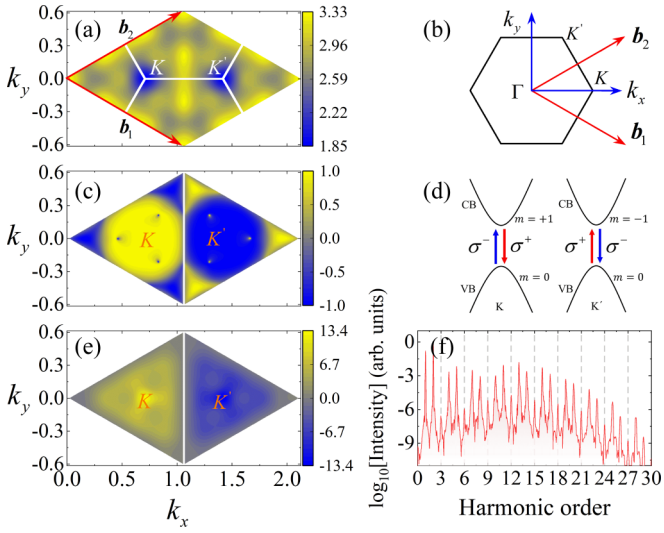

FIG. 1. (a) Band gap (eV) of monolayer MoS_2 in the 2D momentum space, defined as the energy difference between the lowest conduction band (CB) and the highest valence band (VB). The two red arrows represent the two in-plane reciprocal lattice vectors $\mathbf{b}_1 = (\frac{2\pi}{a}, -\frac{2\pi}{\sqrt{3}a})$ and $\mathbf{b}_2 = (\frac{2\pi}{a}, \frac{2\pi}{\sqrt{3}a})$, respectively. $K = (\frac{4\pi}{3a}, 0)$ and $K' = (\frac{8\pi}{3a}, 0)$ are the two inequivalent K points. $a = 3.129$ Å is the lattice constant. (b) The first Brillouin zone in the reciprocal lattice. $\Gamma = (0, 0)$ is the gamma point. The k_x and k_y directions correspond to the zigzag and armchair directions of monolayer MoS_2. (c) Degree of circular polarization. (d) Schematic of one-photon valley-contrasting selection rules: K (K') valley only absorbs left (right) circularly polarized light for the sake of angular momentum conservation. The definition of the polarization: σ^+ (σ^-) correspond to the right (left) circularly polarized state of light. (e) Berry curvature in units of Å^2. (f) Typical total harmonic spectrum driven by CRB fields with (σ^+, σ^-) configuration, that is, σ^+ polarized fundamental and σ^- polarized second harmonic.

experiment [12,22,29] and theory [22,29] show atomic-like monotonic ellipticity dependence. The harmonic yields almost vanishes with CP excitation. Therefore, CHHs cannot be efficiently generated in monolayer MoS_2 crystal excited by a single CP pulses. Fortunately, not only the crystal symmetries, but also the polarization states of the drivers affect HHG from solids [39], it is quite natural to question whether it is possible to generate CHHs in the monolayer MoS_2 crystal by tailored excitation fields and what role will the VSCD play.

The tailored excitation fields can possess desired field symmetries, such as discrete rotational symmetry [5,7]. The selection rules are governed by the associated rotational symmetry of the laser-target system [40–43]. For a system consisting of a laser with L-fold rotational symmetry and a target with in-plane M-fold rotational symmetry, the allowed harmonic orders are $Nk \pm 1 (k = 0, 1, 2, \ldots)$, where N is the greatest common divisor (GCD) of L and M [42,43]. For solid targets with C_M symmetry driven by a single-color CP laser (C_∞ symmetry), the allowed harmonic orders by GCD rule are $Mk \pm 1$, which is consistent with the experimental results [20]. For isotropic gas-phase atoms (C_∞ symmetry) [5] or solid targets with C_3 symmetry [6] driven by the CRB fields with C_3 symmetry, the experimentally observed CHHs orders are $3k \pm 1$, which is consistent with the GCD rule. For solid targets with C_4 or C_6 symmetries, the GCD rule is still valid [6]. Experimental observations show that, similar to gas-phase targets, the lattice itself participates in the HHG process and can give or take angular momentum [6,20], the sum of the angular momentum of the fundamental photons is equal to the angular momentum transferred to the lattice $(Mk, [k \in \mathbb{N}])$ plus the angular momentum of the harmonic photon (± 1) [6,20]. The experimental results also show that the CRB excitation scheme can be used to determine crystal symmetries accurately when the rotational symmetry of the driver and the rotational symmetry of crystal are matched [6].

Recently, lightwave-driven switching of the valley pseudospin on the subcycle scale in a monolayer of tungsten diselenide have shed new light on lightwave valleytronics [44]. In the CRB excitation scheme, a new, robust mechanism for valley selection by the orientation of the trefoil relative to the lattice has been found theoretically [45]. This new mechanism for valley selection induces a sixfold pattern of harmonic emission in graphene with inversion symmetry [26]. Instead, monolayer MoS_2 breaks inversion symmetry, the CRB excitation scheme is expected to imprint VSCD directly onto harmonic spectrum, the two inequivalent valleys will impart different angular momentums to harmonic photons. With the participation of VSCD, what new characteristics will the valley selected harmonic spectrum have?

In this paper, we demonstrate that CHHs can be generated in monolayer MoS_2 with CRB excitation scheme by solving semiconductor Bloch equations (SBEs) in the velocity gauge (VG). The connection between the valley selection of harmonic orders and VSCD is revealed by the valley-resolved and polarization-resolved harmonic spectra. The rotation scanned harmonic spectra clearly show the mechanism of valley selection caused by the trefoil orientation relative to the lattice. Based on the dynamical symmetry analysis, we show that the allowed number of folds in the pattern of direction-dependent yields for above-gap, interband harmonics obey the lowest common multiple (LCM) rule, which provide potential applications to all-optical probes of crystal structure. In addition, we also discover the fingerprints of VSCD leaving in ellipticity of harmonics.

This paper is organized as follows. In Sec. II, we present the details of the SBEs in VG. We illustrate our results and analyze the underlying physical mechanisms in Sec. III. Finally, we summarize the work and draw our conclusions in Sec. IV. Atomic units are used in this paper.

II. THEORETICAL METHODS

In the simulations, we use a symmetry-based (D_{3h} point-group) three-band tight-binding (TB) model for monolayer MoS_2 constructed from a minimal basis consisting of $d_{z^2}, d_{xy}, d_{x^2-y^2}$ orbits of Mo atoms [34] and ignore the spin-orbit coupling. The in-plane C_3 rotational symmetry operations is a subset of the symmetry operations of D_{3h} point-group. Therefore, the Hamiltonian still belongs to the C_3 rotating symmetry. This TB model involving up to the third-nearest-neighbor Mo-Mo hoppings works well in a large neighborhood around the K or K' valley, but it is not enough to capture the physics in the small region around Gamma points where p-orbitals of S atoms are important.

The density matrix approach is used to model the electron dynamics in monolayer MoS_2. Within the independent-particle approximation and the dipole approximation, the temporal evolution of density operator $\hat{\rho}$ is described by SBEs in the VG [28,46–49]

$$\dot{\rho}_{mn}(\mathbf{k},t) = -i\left[\varepsilon_{mn}(\mathbf{k}) - i\frac{1}{T_2}(1-\delta_{mn})\right]\rho_{mn}(\mathbf{k},t) - i\mathbf{A}(t)\cdot\sum_l [\mathbf{P}_{ml}(\mathbf{k})\rho_{ln}(\mathbf{k},t) - \mathbf{P}_{ln}(\mathbf{k})\rho_{ml}(\mathbf{k},t)] - \frac{\rho_{mn}(\mathbf{k},t)-1}{T_1}\delta_{mn}. \quad (1)$$

Here, $\rho_{mn}(\mathbf{k},t)$ is the density matrix element. $\varepsilon_{mn}(\mathbf{k}) = E_m(\mathbf{k}) - E_n(\mathbf{k})$ and $\mathbf{P}_{mn}(\mathbf{k})$ are, respectively, the band-gap energy and the matrix elements of momentum operator between m and n energy bands at $\mathbf{k}$. The diagonal elements of the momentum operator are related to the band dispersion relation by $\mathbf{P}_{nn}(\mathbf{k}) = \nabla_{\mathbf{k}}E_n(\mathbf{k})$. The off-diagonal elements of the momentum operator are calculated as $\mathbf{P}_{mn}(\mathbf{k}) = \gamma\langle n,\mathbf{k}|\nabla_{\mathbf{k}}\hat{H}_{\mathbf{k}}|m,\mathbf{k}\rangle$ where we introduce a factor γ to rescale momentum matrix to *ab initio* result [28], $|m,\mathbf{k}\rangle$ is the periodic part of the Bloch wave function. Different from the way of the damping of physical quantities by the dephasing terms in the length gauge (LG) [47], the dephasing time T_1 and T_2 in Eq. (1) are responsible for the damping of the diagonal and off-diagonal elements of the density matrix, respectively [28,50]. The damping rates for physical qualities such as quantum coherence and population are functions of T_1 and T_2, similar to the mixed form in the literature [51]. Like the dephasing terms in LG, the dephasing terms we used in VG also lead to spectra with clean peaks structure. The advantage of the SBEs in VG is that a random structure gauge is sufficient [28,47–49,52]. The total current in the BZ is

$$\mathbf{J}(t) = \sum_{mn}\int_{\mathrm{BZ}} d\mathbf{k}[\rho_{mn}(\mathbf{k},t)\mathbf{P}_{nm}(\mathbf{k}) + N_{\mathrm{VB}}\mathbf{A}(t)], \quad (2)$$

where N_{VB} is the number of valence bands. The parallelogram defined by nonorthogonal $\mathbf{b}_1$ and $\mathbf{b}_2$ in Fig. 1(a) shows the integral area used in this work, which is equivalent to the first BZ. The high-order harmonic spectrum is given by the Fourier transform (FT) of the time derivative of the current as $I(\omega) \propto \omega^2|\mathrm{FT}[\mathbf{J}(t)]|^2$.

Another advantage of the SBEs in VG is that every $\mathbf{k}$-crystal momentum channel is decoupled [28,46–49], thus making the implementation of parallelization of Eq. (1) more accessible. Meanwhile, K or K' valley-resolved spectra can be reasonably obtained by integrating the Eq. (1) in the left or right triangular region shown in Fig. 1(c). Although the VG require more bands for convergence [47] and the phenomenological dephasing terms are not gauge-invariant [47,53], our simulations ($\gamma = 0.1$, $T_1 = 500$ fs, and $T_2 = 20$ fs [28]) have already captured the orientation-dependent features observed in the experiment [12,54], thus confirming the validity of our simulations.

III. RESULTS AND DISCUSSION

In our simulations, the vector potential of the fields have the following form:

$$A_x(t) = A_0 f(t)\left[\xi_1\cos(\omega t+\varphi) + \frac{R}{q}\xi_2\cos(q\omega t)\right], \quad (3)$$

$$A_y(t) = A_0 f(t)\left[\zeta_1\sin(\omega t+\varphi) + \frac{R}{q}\zeta_2\sin(q\omega t)\right], \quad (4)$$

where A_0 and ω are the amplitude of the vector potential and the circular frequency of the fundamental field, respectively. q is an integer greater than 1, which represents the frequency ratio of the two fields. $\xi_i = \frac{1}{\sqrt{1+\epsilon_i^2}}$, $\zeta_i = \frac{\epsilon_i}{\sqrt{1+\epsilon_i^2}}$, $(i=1,2)$, the negative (positive) ellipticity ϵ_i is defined as the left-handed (right-handed) helicity. The CRB fields ($|\epsilon_i| = 1$, but with opposite signs) composed of the fundamental and its qth harmonic are denoted as $1{:}q$ CRB. It possesses $(q+1)$-fold rotational symmetry, which is denoted as C_{q+1}. We use a temporal envelope $f(t) = \cos^2(\frac{\omega t}{2n})$ with the number of total optical cycles $n = 40$. φ is the phase difference between the two fields. R represents the ratio of the electric field strengths for the CRB fields. The central wavelength 4 μm, peak intensity 1 TW/cm^2 and $R = 2$ are adopted. This laser intensity is below the damage threshold for monolayer MoS_2 [12,22,29].

Figure 1(f) shows the total harmonic spectrum for monolayer MoS_2 driven by $1:2$ CRB fields with (σ^+,σ^-) configuration ($\varphi = 0$). Since C_3 symmetry of $1:2$ CRB fields inherently conform to the threefold rotation symmetry of monolayer MoS_2, the harmonics come in pairs, $n(\omega+2\omega)+\omega = (3n+1)\omega$ and $n(\omega+2\omega)+2\omega = (3n+2)\omega$, which is consistent with the GCD rule and is similar with the result from neon or argon gas [5,7,8] or pristine graphene [26] exposed to $1:2$ CBR fields. The distinguishing feature is that the harmonics $3n\omega$ are no longer parity forbidden, reflecting the broken inversion symmetry. But the intensity of the harmonics $3n\omega$ is about three orders of magnitude lower than that of harmonics $(3n+1)\omega$ and $(3n+2)\omega$.

A. Valley-selective HHG

Figure 2(a1) shows the left (σ^-) and right (σ^+) circularly polarized components of the harmonic emission driven by $1:2$ CRB fields with (σ^+,σ^-) configuration. The 10th and 13th [$(3n+1)$th] harmonics are dominant by σ^- components, whereas the 11th and 14th [$(3n+2)$th] harmonics are dominant by σ^+ components. Therefore, the $(3n+1)$th and $(3n+2)$th harmonics are nearly circular with opposite helicity. But, for the $3n$th harmonics such as H12, the intensity of σ^- component is comparable to that of σ^+ component, and therefore are not circular. When drivers with (σ^-,σ^+) configuration are used, as shown in Fig. 2(b1), except for the reversal of harmonic helicity, other characteristics remain unchanged.

Valley-resolved total spectra in Fig. 2(a2) show that the intensity of the K-valley components for the 11th and 14th [$(3n+2)$th] are much higher than that of the K'-valley components. While for the 10th and 13th [$(3n+1)$th], the situation is reversed. These results support that, for (σ^+,σ^-) configuration drivers, the 11th and 14th [$(3n+2)$th] harmonics are emitted from the K valley, while the 10th and 13th

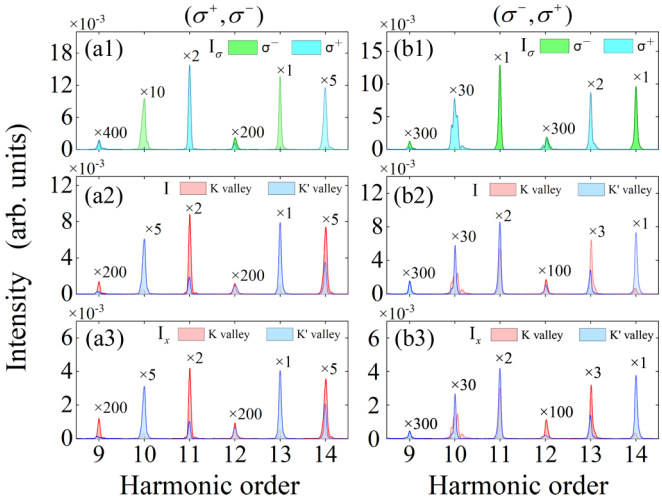

FIG. 2. HHG spectra from monolayer MoS_2 driven by 1 : 2 CRB fields ($\varphi = 0$). Green (cyan) shaded areas indicate σ^+-polarized (σ^--polarized) spectra, respectively. Red (blue) shaded areas indicate K valley (K' valley) resolved spectra, respectively. Individual harmonic orders are multiplied with the indicated multiplication factors. (a1)–(a3) HHG spectra driven by 1 : 2 CRB fields with (σ^+, σ^-) configuration. (b1)–(b3) HHG spectra driven by 1 : 2 CRB fields with (σ^-, σ^+) configuration. (a1,b1) σ^+ (σ^-) components of the total harmonic spectra. (a2,b2) Valley-resolved total harmonic spectra. (a3,b3) Valley-resolved, x-polarized components of total harmonic spectra.

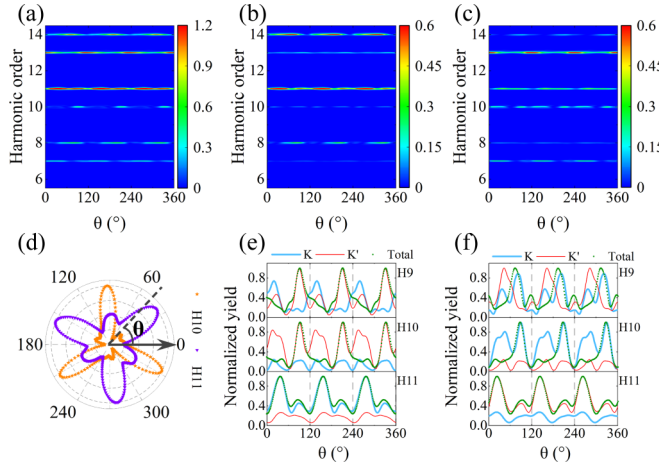

FIG. 3. (a) The total harmonic spectra as a function of the angle θ. Panels (b) and (c) show the K and K' valley-resolved spectra as a function of the angle θ on the same scale (not logarithmic). Panel (d) shows the polarplot of the normalized yields for H10 (orange five-pointed stars) and H11 (violet triangles) as a function of angle θ. The angle θ denote the orientation of the 1 : 2 CRB fields with respect to Γ–K direction (dark gray arrow, 0° direction). Panels (e) and (f) show the normalized harmonic yields as a function of the angle θ, calculated for the total and valley-resolved ninth, tenth, and 11th harmonics. Thick cyan (thin red) lines represent harmonic yields for K (K') valley-resolved harmonics. Yields for a specific order of valley-resolved harmonics are normalized by the maximum yield between the yield of K and yield of K' valley. Yields for a specific order of total harmonics (olive green circles) are normalized independently. Panels (a)–(e) are spectra driven by fields with (σ^+, σ^-) configuration. Panel (f) represents spectra driven by fields with (σ^-, σ^+) configuration.

[$(3n + 1)$th] harmonics are emitted from the K' valley. When drivers with (σ^-, σ^+) configuration are used, the intensity ratio of K to K' valley components is reversed [Fig. 2(b2)]. The x-polarized spectra shown in Figs. 2(a3) and 2(b3) support the same conclusion. The one-to-one relationship between the reversal of the helicity and the reversal of valley-resolved origins support that the valley selection of harmonic orders occur in monolayer MoS_2 with broken inversion symmetry, the generation of $(3n + 1)$th and $(3n + 2)$th harmonics follows the one-photon valley-contrasting selection rules, as shown in Fig. 1(d), when the recombinations of electron-hole pair occur in the K valley (K' valley), the interband harmonics will have right (left) circular polarization for the sake of angular momentum conservation. Therefore the $(3n + 1)$th and $(3n + 2)$th harmonics are dominant by the interband mechanism and the distinctive valley selection of harmonic orders can be attributed to the VSCD of monolayer MoS_2. Note that the valley selection of harmonic orders cannot occur in the inversion-symmetric graphene system [26]. The only exception for the valley-resolved spectra of H10 in Figs. 1(b2) and 2(b3) will be discussed in the following analysis.

Figures 3(a)–3(c) present, respectively, the simulated total, K, and K' valley-resolved spectra driven by 1 : 2 CRB field with (σ^+, σ^-) configuration as a function of the trefoil orientation angle relative to the lattice. Three features are worth mentioning. The first is the valley selection of harmonic orders, that is, $(3n + 1)$th harmonics [$n = 2, 3, 4$ in Fig. 3] mainly comes from the contribution of the K' valley, and the contribution of the K valley is small. Whereas the $(3n + 2)$th harmonics are dominated by the contribution of the K valley. Figure 3(e) shows the valley selection of harmonic orders more clearly. Figure 3(f) show that the reversed results are observed when simultaneously changing the helicities of both driving fields. Second, as shown in Figs. 3(a) and 3(d), the valleys (harmonic orders) are also selected by the orientation of the CRB fields relative to the lattice (each 180° change in φ results in 120° rotation of the 1 : 2 CRB fields). Figure 3(d) clearly shows that the H11 (violet triangles) are mainly emitted with the orientation of the CRB fields along the Γ-M directions ($\theta = 30°, 150°, 270°$), approximately. While the orientation of the CRB fields along the Γ-M directions ($\theta = 90°, 210°, 330°$), approximately, are favored for H10 (orange five-pointed stars). Third, each pair of harmonics (specific n value) exhibit three-fold beating similar to Fig. 3(d), but with different offset phases. The similar phase offset was observed in quartz by experiments [6]. It can be qualitatively understood by the recollision model for HHG in solids [55–63], the electron-hole pairs generated at different initial momentum go across different recollision trajectories, thus accumulating a different dynamic phase [64–66], leading to different offset phases for different pairs of harmonics. Otherwise, the valley selection caused by field orientation can be used to obtain helicity-selected harmonics in a wide spectral range. Furthermore, as shown in Fig. 3(f), the yields of H10 for K and K' valley-resolved components are nearly equal (near zero) at $\theta = 0°, 120°, 240°, 360°$, corresponding

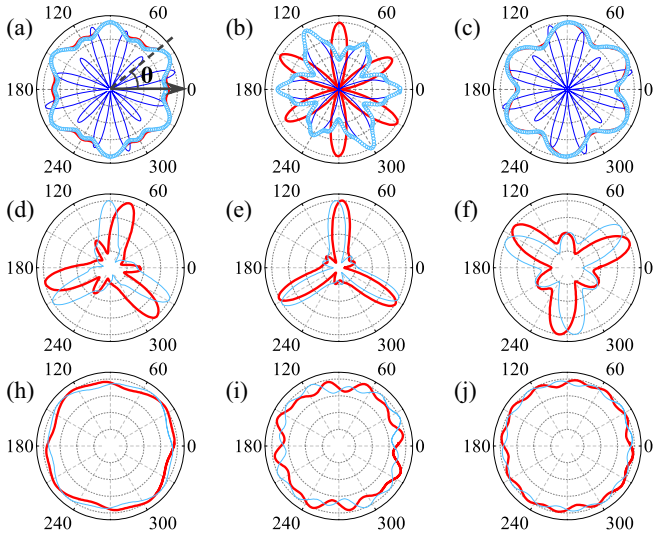

FIG. 4. (a)–(c) Yields of the total harmonics (cyan open circles), the parallel (thick red lines), and perpendicular (thin blue lines) components of harmonics as a function of angle θ for LP laser. (d)–(f) Yields of harmonics as a function of the angle θ for 1 : 2 CRB fields. (h)–(i) Yields of harmonics as a function of the angle θ for 1 : 3 CRB fields. Thick red lines and thin cyan lines in panels (d)–(j) are driven by CRB fields with (σ^-, σ^+) configuration and (σ^+, σ^-) configuration, respectively. The angle θ denote the polarization direction of LP field or the orientation of the CRB fields with respect to Γ-K direction (dark gray arrow, 0° direction). First [(a), (d), and (h)], second [(b), (e), and (i)], and third [(c), (f), and (j)] columns present the normalized, direction-resolved yields of harmonics for ninth (H9), tenth (H10), and 11th (H11) harmonic orders, respectively. Note that the yields of harmonics are normalized independently.

to the exception for H10 in Figs. 2(b2) and 2(b3). Except for these points, the yield of the K-valley component are always greater than that of the K'-valley component. Therefore, the exception for H10 in Figs. 2(b2) and 2(b3) do not change the qualitative conclusions about the valley selection of harmonic orders.

B. Rotational symmetry probing via dynamical symmetry

To investigate the dependence of HHG on the dynamical symmetries, we apply the LP field, 1 : 2 CRB fields, and 1 : 3 CRB fields, corresponding to C_2, C_3, and C_4 symmetries, respectively, to the monolayer MoS_2. The polar plots of the normalized yields of the total, parallel, and perpendicular components for H9, H10, and H11 (above-gap harmonics) driving by LP laser pulses are shown in Figs. 4(a)–4(c), respectively. The parallel components (thick red lines) exhibit a sixfold pattern. The perpendicular components (thin blue lines) of even harmonics also exhibit a clear sixfold pattern, whereas the perpendicular components (thin blue lines) of odd harmonics exhibit a twelvefold pattern. The total yields of odd harmonics are mainly contributed to by parallel components, whereas the total yields of even harmonics are dominated by perpendicular components. Both the total yields (cyan open circles) of odd and even harmonics exhibit a sixfold pattern. The LP laser field possesses C_2 symmetry, and the monolayer MoS_2 possesses C_3 symmetry, the allowed number of lobes in the pattern of total yields are the LCM of rotational symmetries of the target and laser field. All of these polarization-dependent results reported in Figs. 4(a)–4(c) are in excellent agreement with the experimental observation [12] and the recent theoretical simulation [28], thus validating our calculations.

When 1 : 2 CRB fields are used, the C_3 symmetry of the field exactly matches the C_3 symmetry of monolayer MoS_2. The convolution of the threefold field and the threefold crystal result in a threefold pattern, which are clearly demonstrated in the polar plots of the normalized yields for H9, H10, and H11 in Figs. 4(d)–4(f). The thin cyan lines for the (σ^+, σ^-) configuration are extracted from the spectrograms in Fig. 3(a). The maximal yields of H10 are along the Γ-M directions ($\theta = 90°, 210°, 330°$), approximately. The maximal yields of H11 are along the Γ-M directions ($\theta = 30°, 150°, 270°$), approximately. In addition, there are three unexpected, small lobes (sublobes) displaced by 60° relative to the three main lobes, e.g., the sublobes are along the 90°, 210°, 330° directions in Fig. 4(f). Notably, thin cyan lines and thick red lines, are mirror symmetrical to the Γ-M directions, approximately. The threefold patterns for H9 are obviously different from that of H10 and H11. The maximal yields for the (σ^-, σ^+) configuration (the thick red line for H9) deviates from the Γ-M direction, neither in the Γ-M direction nor in the Γ-K direction. The mirror symmetry between the thick red line and the thin cyan line for H9 no longer exists. All in all, the allowed number of lobes is still equal to the LCM of the rotational symmetries of the target and laser fields.

If the rotational symmetry of the target and laser fields do not match exactly, what will the pattern of direction-dependent yields look like? Figures 4(i) and 4(j) show the normalized total yields of H10 and H11 for 1 : 3 CRB fields with C_4 symmetry and the monolayer MoS_2 with the C_3 symmetry, where the ambiguous twelvefold pattern with a small modulation depth is observed. These expected results further confirm the LCM rule. However, the yield pattern of H9 ($3n$th harmonic) is closer to a fourfold symmetry. Note that each 120° change in φ results in 90° rotation of the 1 : 3 CRB fields.

LCM rules can be well understood by a real-space picture for HHG in solids [11,15,67]. Since monolayer MoS_2 is a layered material with a hexagonal lattice, it has three in-plane S-Mo bonds. The spatial directions of atomic bonds define the preferred directions for electronic motion in real space [11,15,67]. The harmonic yields are maximized when the exciting electric field is aligned with these preferred directions [11,15,67]. Therefore, when we discuss the rotational symmetry of the pattern of direction-dependent harmonic yields, we are actually faced with a counting problem [68]. When the laser field rotate by 360° around the axis of laser propagation, we need to count the number of times that the lobes of the electric field are aligned with the direction of the S-Mo bond (abbreviated as the LABD event), which equals the number of folds for the rotational symmetry of the yield pattern. Note that the lobes of the laser electric field have the same rotational symmetry with the laser vector potential in momentum space.

In general, for a system consisting of a laser with L-fold rotational symmetry and a target with in-plane M-fold

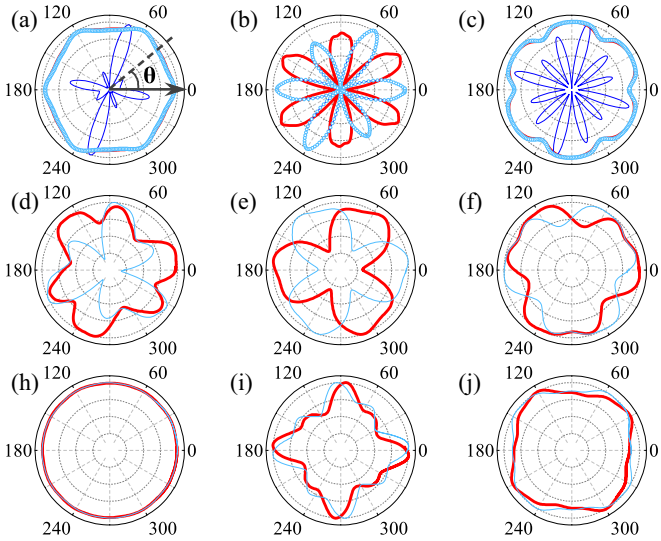

FIG. 5. The same as Fig. 4 but for below-gap harmonics H3, H4, and H5.

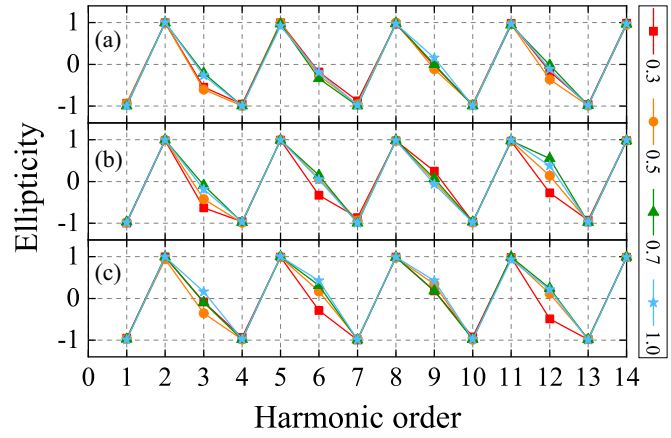

FIG. 6. Ellipticity of harmonics driven by fields with (σ^+, σ^-) configuration with $\epsilon_2 = 1.0$ and $\epsilon_1 = 0.3, 0.5, 0.7, 1.0$, respectively. Panels (a), (b), and (c) are ellipticity of harmonics for $\theta = 0^\circ, 30^\circ, 60^\circ$, respectively.

rotational symmetry, the total number of LABD events should be $L \times M$. When the GCD of L and M is greater than 1, i.e., GCD > 1, the LABD events always occur simultaneously for GCD lobes. Thus, the GCD LABD events are indistinguishable. According to the Addition Principle [68], the number of the LABD events is $L \times M/\text{GCD} = \text{LCM}$.

For the below-gap harmonics driving by LP laser pulses, as shown in Figs. 5(a)–5(c), in addition to minor differences in the details, the yield pattern and characteristics are consistent with those of the above-gap harmonics. For the case of fields with C_3 symmetry, as shown in Figs. 5(e) and 5(f), the normalized total yields of H4 and H5 still exhibit a threefold pattern, but with relatively wider lobes and thus ambiguous directivities. Obviously, the mirror symmetries to Γ-M directions between the thick red lines and the thin cyan lines are preserved. For the below-gap H3 ($3n$th harmonic), the unexpected sublobes become too big to be identified as a threefold pattern [Fig. 5(d)]. For the case of fields with C_4 symmetry, the below-gap H3 shows a near isotropic yield pattern, and the yield patterns of H4 and H5 are closer to a fourfold symmetry.

To sum up, only the above-gap, interband harmonics obey the LCM rule, while the above-gap $3n$th harmonics and the below-gap harmonics do not. Therefore, for the purpose of structural probing, it is preferable to use above-gap, interband harmonics, e.g., $(3n+1)$th or $(3n+2)$th harmonics, its narrower lobes and the larger modulation depths in the orientation-dependent pattern of the harmonic yield reduce the experimental challenges, make this all-optical method for structural probes more promising. More generally, when the crystal symmetry is unknown, the LCM rule mean that one should use the combination of different excitation schemes to decode the rotation symmetries of crystal with HHG. For example, a polarization scan with a LP field will lead to sixfold pattern for both targets of C_3 and C_6 symmetries, while a polarization scan with threefold fields will lead to sixfold pattern for both targets of C_2 and C_6 symmetries. Therefore, the combination of LP field scheme and threefold fields scheme is essential to make an accurate judgment about the rotation symmetry of crystal.

C. Fingerprints of VSCD leaving in harmonic spectra

Figure 6 shows that the ellipticity of the $3n$th harmonics can be adjusted by tuning the ellipticity of one of the driving fields, ϵ_1, whereas the ellipticity of the $(3n+1)$th and $(3n+2)$th harmonics hardly changes. This is dramatically different from that of the gas medium, where the ellipticity of every harmonics can be controlled by varying the ellipticity of the driving lasers [7]. So far, it is generally accepted that the HHG in solids is contributed to by two distinct mechanisms: the interband mechanism and the intraband mechanism. The sensitivity of the harmonic ellipticity to the driver's ellipticity can be qualitatively understood by which mechanism dominates for a particular harmonic order.

The interband mechanisms are better understood in terms of the polarization of the electron-hole pairs or the recollision picture, while the intraband mechanism can be understood by the semiclassical motion of carriers (e.g., on the mth band) driving by the laser field

$$\mathbf{v}_m(\mathbf{k}) = \nabla_{\mathbf{k}}\varepsilon_m(\mathbf{k}) + \mathbf{E}(t) \times \Omega_m(\mathbf{k}). \tag{5}$$

The first term of the above equation is the group velocity of the mth band, the second term is the transverse velocity induced by Berry curvature. Naturally, the intraband current can be written in the following two parts:

$$\begin{aligned}\mathbf{J}(t) &= \int_{\text{BZ}} \mathbf{v}_m[\mathbf{k}(t)] n_m(\mathbf{k}, t) d^2\mathbf{k} \\ &= \int_{\text{BZ}} \nabla_{\mathbf{k}}\varepsilon_m[\mathbf{k}(t)] n_m(\mathbf{k}, t) d^2\mathbf{k} \\ &\quad + \int_{\text{BZ}} \mathbf{E}(t) \times \mathbf{\Omega}_m[\mathbf{k}(t)] n_m(\mathbf{k}, t) d^2\mathbf{k} \\ &= \mathbf{J}_v(t) + \mathbf{J}_{\text{BC}}(t),\end{aligned} \tag{6}$$

where $\mathbf{J}_v(t)$ represents the intraband current generated by group velocity of the mth band, $\mathbf{J}_{\text{BC}}(t)$ corresponds to the

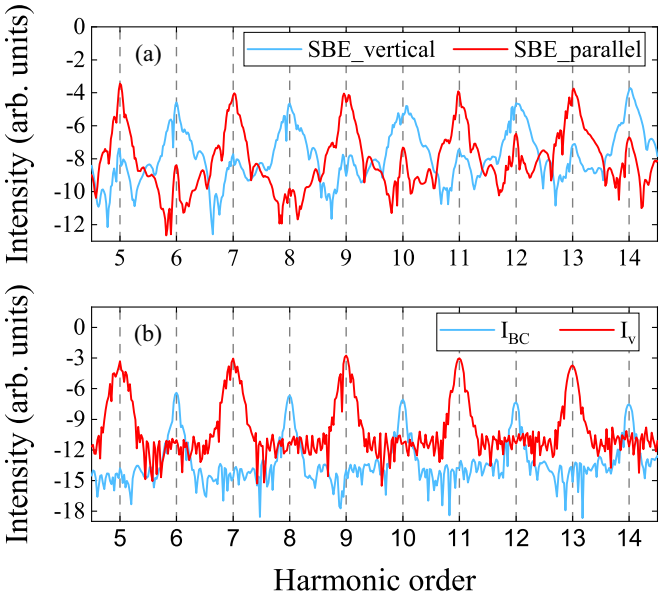

FIG. 7. Harmonic spectrum from monolayer MoS_2 driving by linearly polarized laser field with $\theta = 60^\circ$. (a) The perpendicular (cyan solid line) and parallel (red dashed line) components of high harmonics obtained by solving three-band SBEs in VG. (b) The harmonic spectrum obtained by the 2D single-band model. The cyan line and red line represent the harmonic components of $\mathbf{J}_{\mathrm{BC}}(t)$ and $\mathbf{J}_v(t)$, respectively.

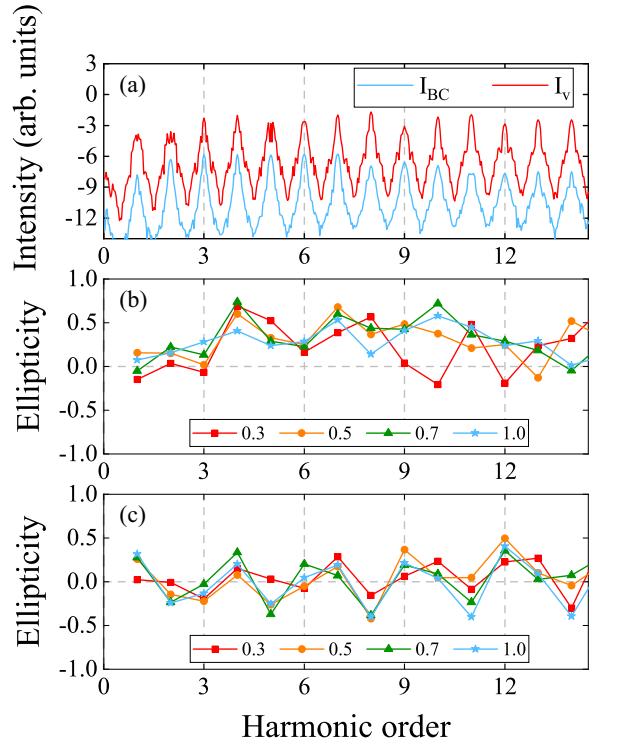

FIG. 8. (a) Harmonic spectrum from monolayer MoS_2 driving by $1:2$ CRB fields with (σ^+, σ^-) configuration and $\theta = 60^\circ$ obtained by the 2D single-band model. The cyan line and red line represent the harmonic components of $\mathbf{J}_{\mathrm{BC}}(t)$ and $\mathbf{J}_v(t)$, respectively. (b) Ellipticity of harmonics components induced by $\mathbf{J}_{\mathrm{BC}}(t)$ driven by $1:2$ CRB fields with (σ^+, σ^-) configuration with $\epsilon_2 = 1.0$ and $\epsilon_1 = 0.3, 0.5, 0.7, 1.0$, respectively. (c) The same as panel (b) but for harmonics components induced by $\mathbf{J}_v(t)$.

anomalous intraband current generated by the transverse velocity-induced by Berry curvature.

To gain insights on the effect of $\mathbf{J}_v(t)$ and $\mathbf{J}_{\mathrm{BC}}(t)$, we assume a uniform distribution of carriers, i.e., $n_v[k(t)] \approx 1$, and perform single-band (valence band) calculations. As shown in Fig. 7, even if the distribution of carriers is ignored, our single-band simulations still capture the essential features of the effect of the group velocity of valence-band and Berry curvature: Berry curvature induces a transverse current and hence the even harmonics, while the group velocity of the valence band only causes odd-order harmonics [12,28,50].

When $1:2$ CRB fields are used, as shown in Fig. 8(a), both the Berry curvature and group velocity of the valence band contribute to the generation of odd and even harmonics. Figures 8(b) and 8(c) show that whether it is the harmonic generated by Berry curvature or the harmonic generated by group velocity of valence, its ellipticity is sensitively dependent on ϵ_1. This result can be understood as follows: At different ϵ_1 the vector potentials of the fields have different Lissajous figures, leading to different reciprocal space trajectories, as shown in Fig. 1, the energy landscape or Berry curvature felt by carriers with different reciprocal space trajectories have different values, resulting in different intraband currents, and thus the harmonic ellipticities are sensitive to ϵ_1. Note that, based on these single-band simulations, we cannot quantitatively judge which of the $\mathbf{J}_v(t)$ and $\mathbf{J}_{\mathrm{BC}}(t)$ is dominated. On the contrary, the emission process of interband harmonics follow the one-photon valley-contrasting selection rules. As shown in Fig. 1(c), the DCP have values close to 1 (-1) in a large neighborhood of the K (K') point. Although different reciprocal space trajectories lead to different positions of recombination, there is a great possibility that the DCP at different positions of recombination have the same value. For this reason, the harmonics of interband mechanism are insensitive to the ellipticity of the driving field.

The interband mechanism of the $3n$th harmonics are forbidden by the GCD rule, the only physical origin of $3n$th harmonics is the intraband current. The above analysis implies that its ellipticities are sensitive to ϵ_1. This is exactly the characteristic of the $3n$th harmonics obtained by the SBEs simulations (shown in Fig. 6). Unlike the $3n$th harmonics, both interband and intraband mechanisms contribute to the $(3n+1)$th and $(3n+2)$th harmonics. If and only if the interband mechanism is dominant, the sensitivity of the ellipticities of the intraband harmonic to the drivers ellipticity will be masked; this is exactly the characteristic of the $(3n+1)$th and $(3n+2)$th harmonics obtained by the SBEs simulations. Indeed, SBEs simulations show that the intensity of the $(3n+1)$th and $(3n+2)$th harmonics is about three orders of magnitude higher than that of the $3n$th harmonics (shown in Fig. 1).

The above analysis implies that the insensitivity of the harmonic ellipticity to the driver's ellipticity reveals unique fingerprints of VSCD in the harmonic spectra of monolayer MoS_2.

IV. CONCLUSION

In summary, we show that the efficient generation of CHHs can be achieved in monolayer MoS_2 with $1:2$ CRB fields. The primary spectral characteristic is that the interband harmonics come in pairs with opposite helicity. The distinguishing feature is the emission of intraband $3n$ ($n \in \mathbb{N}$) harmonic orders due to the broken inversion symmetry. Specifically, both the valley selection caused by the trefoil orientation relative to the lattice and the valley selection of harmonic orders via valley-contrasting selection rule are observed. For the purpose of structural probing, we show that it is preferable to use above-gap, interband harmonics. According to the dynamical symmetry analyses, the combination of the LP excitation scheme and CRB excitation scheme is sufficient to decode the possible rotation symmetries of the crystal (C_m, $m = 1, 2, 3, 4, 6$). Moreover, the insensitivity of the harmonic ellipticity to the driver's ellipticity unveils the unique fingerprints of the VSCD in HHG. In the future, the controllable valley polarization may allow for the production of the helicity-selective harmonics, as well as the generation of isolated circularly polarized attosecond pulses. The present work offers a route to strong-field valley-selected processes in 2D materials with broken inversion symmetry.

ACKNOWLEDGMENTS

We sincerely thank Prof. Hongchuan Du from Lanzhou University for helpful discussions. This work was supported by the National Natural Science Foundation of China (Grants No. 12074146, No. 12074142, No. 11464010, and No. 11964008).

[1] R. Cireasa, A. E. Boguslavskiy, B. Pons, M. C. H. Wong, D. Descamps, S. Petit, H. Ruf, N. Thiré, A. Ferré, J. Suarez, J. Higuet, B. E. Schmidt, A. F. Alharbi, F. Légaré, V. Blanchet, B. Fabre, S. Patchkovskii, O. Smirnova, Y. Mairesse, and V. R. Bhardwaj, Nat. Phys. **11**, 654 (2015).

[2] T. Fan, P. Grychtol, R. Knut, C. Hernández-García, D. D. Hickstein, D. Zusin, C. Gentry, F. J. Dollar, C. A. Mancuso, C. W. Hogle, O. Kfir, D. Legut, K. Carva, J. L. Ellis, K. M. Dorney, C. Chen, O. G. Shpyrko, E. E. Fullerton, O. Cohen, P. M. Oppeneer, D. B. Milošević, A. Becker, A. A. Jaroń-Becker, T. Popmintchev, M. M. Murnane, and H. C. Kapteyn, Proc. Natl. Acad. Sci. U.S.A. **112**, 14206 (2015).

[3] A. Ferré, C. Handschin, M. Dumergue, F. Burgy, A. Comby, D. Descamps, B. Fabre, G. A. Garcia, R. Géneaux, L. Merceron, E. Mével, L. Nahon, S. Petit, B. Pons, D. Staedter, S. Weber, T. Ruchon, V. Blanchet, and Y. Mairesse, Nat. Photonics **9**, 93 (2015).

[4] O. Travnikova, J.-C. Liu, A. Lindblad, C. Nicolas, J. Söderström, V. Kimberg, F. Gel'mukhanov, and C. Miron, Phys. Rev. Lett. **105**, 233001 (2010).

[5] O. Kfir, P. Grychtol, E. Turgut, R. Knut, D. Zusin, D. Popmintchev, T. Popmintchev, H. Nembach, J. M. Shaw, A. Fleischer, H. Kapteyn, M. Murnane, and O. Cohen, Nat. Photonics **9**, 99 (2015).

[6] T. Heinrich, M. Taucer, O. Kfir, P. B. Corkum, A. Staudte, C. Ropers, and M. Sivis, Nat. Commun. **12**, 3723 (2021).

[7] A. Fleischer, O. Kfir, T. Diskin, P. Sidorenko, and O. Cohen, Nat. Photonics **8**, 543 (2014).

[8] L. Medišauskas, J. Wragg, H. van der Hart, and M. Y. Ivanov, Phys. Rev. Lett. **115**, 153001 (2015).

[9] D. D. Hickstein, F. J. Dollar, P. Grychtol, J. L. Ellis, R. Knut, C. Hernández-García, D. Zusin, C. Gentry, J. M. Shaw, T. Fan, K. M. Dorney, A. Becker, A. Jaroń-Becker, H. C. Kapteyn, M. M. Murnane, and C. G. Durfee, Nat. Photonics **9**, 743 (2015).

[10] X. Zhou, R. Lock, N. Wagner, W. Li, H. C. Kapteyn, and M. M. Murnane, Phys. Rev. Lett. **102**, 073902 (2009).

[11] F. Langer, M. Hohenleutner, U. Huttner, S. W. Koch, M. Kira, and R. Huber, Nat. Photonics **11**, 227 (2017).

[12] H. Liu, Y. Li, Y. S. You, S. Ghimire, T. F. Heinz, and D. A. Reis, Nat. Phys. **13**, 262 (2017).

[13] T. T. Luu and H. J. Wörner, Nat. Commun. **9**, 916 (2018).

[14] K. Kaneshima, Y. Shinohara, K. Takeuchi, N. Ishii, K. Imasaka, T. Kaji, S. Ashihara, K. L. Ishikawa, and J. Itatani, Phys. Rev. Lett. **120**, 243903 (2018).

[15] S. Jiang, S. Gholam-Mirzaei, E. Crites, J. E. Beetar, M. Singh, R. Lu, M. Chini, and C. D. Lin, J. Phys. B: At. Mol. Opt. Phys. **52**, 225601 (2019).

[16] K. Uchida, V. Pareek, K. Nagai, K. M. Dani, and K. Tanaka, Phys. Rev. B **103**, L161406 (2021).

[17] N. Klemke, N. Tancogne-Dejean, G. M. Rossi, Y. Yang, F. Scheiba, R. Mainz, G. Di Sciacca, A. Rubio, F. Kärtner, and O. Mücke, Nat. Commun. **10**, 1319 (2019).

[18] N. Klemke, O. D. Mücke, A. Rubio, F. X. Kärtner, and N. Tancogne-Dejean, Phys. Rev. B **102**, 104308 (2020).

[19] N. Tancogne-Dejean, O. D. Mücke, F. X. Kärtner, and A. Rubio, Nat. Commun. **8**, 745 (2017).

[20] N. Saito, P. Xia, F. Lu, T. Kanai, J. Itatani, and N. Ishii, Optica **4**, 1333 (2017).

[21] T. T. Luu and H. J. Wörner, Eur. Phys. J.: Spec. Top. (2021), doi: 10.1140/epjs/s11734-021-00278-8.

[22] N. Yoshikawa, T. Tamaya, and K. Tanaka, Science **356**, 736 (2017).

[23] M. Taucer, T. J. Hammond, P. B. Corkum, G. Vampa, C. Couture, N. Thiré, B. E. Schmidt, F. Légaré, H. Selvi, N. Unsuree, B. Hamilton, T. J. Echtermeyer, and M. A. Denecke, Phys. Rev. B **96**, 195420 (2017).

[24] M. Baudisch, A. Marini, J. D. Cox, T. Zhu, F. Silva, S. Teichmann, M. Massicotte, F. Koppens, L. S. Levitov, F. J. García de Abajo, and J. Biegert, Nat. Commun. **9**, 1018 (2018).

[25] Z.-Y. Chen and R. Qin, Opt. Express **27**, 3761 (2019).

[26] M. S. Mrudul, Álvaro Jiménez-Galán, M. Ivanov, and G. Dixit, Optica **8**, 422 (2021).

[27] Ó. Zurrón-Cifuentes, R. Boyero-García, C. Hernández-García, A. Picón, and L. Plaja, Opt. Express **27**, 7776 (2019).

[28] C. Liu, Y. Zheng, Z. Zeng, and R. Li, New J. Phys. **22**, 073046 (2020).

[29] Z. Lou, Y. Zheng, C. Liu, L. Zhang, X. Ge, Y. Li, J. Wang, Z. Zeng, R. Li, and Z. Xu, Opt. Commun. **469**, 125769 (2020).

[30] J. Cao, F. Li, Y. Bai, P. Liu, and R. Li, Opt. Express **29**, 4830 (2021).

[31] C. Yu, S. Jiang, T. Wu, G. Yuan, Y. Peng, C. Jin, and R. Lu, Phys. Rev. B **102**, 241407(R) (2020).

[32] Z. Wang, S. Jiang, G. Yuan, T. Wu, C. Li, C. Qian, C. Jin, C. Yu, W. Hua, and R. Lu, Sci. China Phys. Mech. Astron. **63**, 257311 (2020).

[33] H. D. Yao, B. Cui, M. S. Qi, C. Yu, and R. Lu, Acta Phys. Sin. **70**, 134207 (2021).

[34] G.-B. Liu, W.-Y. Shan, Y. Yao, W. Yao, and D. Xiao, Phys. Rev. B **88**, 085433 (2013).

[35] D. Xiao, G.-B. Liu, W. Feng, X. Xu, and W. Yao, Phys. Rev. Lett. **108**, 196802 (2012).

[36] T. Cao, G. Wang, W. Han, H. Ye, C. Zhu, J. Shi, Q. Niu, P. Tan, E. Wang, B. Liu, and J. Feng, Nat. Commun. **3**, 887 (2012).

[37] K. F. Mak, K. He, J. Shan, and T. F. Heinz, Nat. Nanotechnol. **7**, 494 (2012).

[38] H. Zeng, J. Dai, W. Yao, D. Xiao, and X. Cui, Nat. Nanotechnol. **7**, 490 (2012).

[39] G.-R. Jia, X.-Q. Wang, T.-Y. Du, X.-H. Huang, and X.-B. Bian, J. Chem. Phys. **149**, 154304 (2018).

[40] O. E. Alon, V. Averbukh, and N. Moiseyev, Phys. Rev. Lett. **80**, 3743 (1998).

[41] F. Mauger, A. D. Bandrauk, and T. Uzer, J. Phys. B: At. Mol. Opt. Phys. **49**, 10LT01 (2016).

[42] X. Liu, X. Zhu, L. Li, Y. Li, Q. Zhang, P. Lan, and P. Lu, Phys. Rev. A **94**, 033410 (2016).

[43] K.-J. Yuan and A. D. Bandrauk, Phys. Rev. A **97**, 023408 (2018).

[44] F. Langer, C. P. Schmid, S. Schlauderer, M. Gmitra, J. Fabian, P. Nagler, C. Schüller, T. Korn, P. G. Hawkins, J. T. Steiner, U. Huttner, S. W. Koch, M. Kira, and R. Huber, Nature (London) **557**, 76 (2018).

[45] Á. Jiménez-Galán, R. E. F. Silva, O. Smirnova, and M. Ivanov, Nat. Photonics **14**, 728 (2020).

[46] G. Ernotte, T. J. Hammond, and M. Taucer, Phys. Rev. B **98**, 235202 (2018).

[47] L. Yue and M. B. Gaarde, Phys. Rev. A **101**, 053411 (2020).

[48] D. Kim, D. Shin, A. S. Landsman, D. E. Kim, and A. Chacón, arXiv:2105.12294.

[49] J. Cao, N. Li, Y. Bai, P. Liu, and R. Li, Chin. Opt. Lett. **19**, 043201 (2021).

[50] Z. Lou, Y. Zheng, C. Liu, Z. Zeng, R. Li, and Z. Xu, Opt. Express **29**, 37809 (2021).

[51] R. W. Boyd, *Nonlinear Optics*, 4th ed. (Academic, New York, 2020), pp. 137–202.

[52] S. Jiang, C. Yu, J. Chen, Y. Huang, R. Lu, and C. D. Lin, Phys. Rev. B **102**, 155201 (2020).

[53] M. Du, C. Liu, Z. Zeng, and R. Li, Phys. Rev. A **104**, 033113 (2021).

[54] R. Hollinger, L. Yue, C. B. Uzundal, Z. Gan, A. George, C. Spielmann, D. Kartashov, A. Turchanin, D. Y. Qiu, M. B. Gaarde, and M. Zuerch, *OSA Nonlinear Optics 2021* (Optical Society of America, Washington, D.C., 2021), p. NW2A.4.

[55] G. Vampa, C. R. McDonald, G. Orlando, D. D. Klug, P. B. Corkum, and T. Brabec, Phys. Rev. Lett. **113**, 073901 (2014).

[56] G. Vampa, C. R. McDonald, G. Orlando, P. B. Corkum, and T. Brabec, Phys. Rev. B **91**, 064302 (2015).

[57] L. Li, P. Lan, X. Zhu, T. Huang, Q. Zhang, M. Lein, and P. Lu, Phys. Rev. Lett. **122**, 193901 (2019).

[58] L. Yue and M. B. Gaarde, Phys. Rev. Lett. **124**, 153204 (2020).

[59] T. Ikemachi, Y. Shinohara, T. Sato, J. Yumoto, M. Kuwata-Gonokami, and K. L. Ishikawa, Phys. Rev. A **95**, 043416 (2017).

[60] X. Zhang, J. Li, Z. Zhou, S. Yue, H. Du, L. Fu, and H.-G. Luo, Phys. Rev. B **99**, 014304 (2019).

[61] S. Fu, Y. Feng, J. Li, S. Yue, X. Zhang, B. Hu, and H. Du, Phys. Rev. A **101**, 023402 (2020).

[62] L. Yue and M. B. Gaarde, Phys. Rev. A **103**, 063105 (2021).

[63] Y.-L. He, J. Guo, F.-Y. Gao, Z.-J. Yang, S.-Q. Zhang, and X.-S. Liu, Phys. Rev. A **104**, 013104 (2021).

[64] G. Vampa, T. J. Hammond, N. Thiré, B. E. Schmidt, F. Légaré, C. R. McDonald, T. Brabec, D. D. Klug, and P. B. Corkum, Phys. Rev. Lett. **115**, 193603 (2015).

[65] T. T. Luu and H. J. Wörner, Phys. Rev. A **98**, 041802(R) (2018).

[66] T. T. Luu and H. J. Wörner, Phys. Rev. B **94**, 115164 (2016).

[67] Y. Morimoto, Y. Shinohara, M. Tani, B.-H. Chen, K. L. Ishikawa, and P. Baum, Optica **8**, 382 (2021).

[68] K. M. Koh and E. G. Tay, *Counting*, 2nd ed. (World Scientific, Singapore, 2013).